

# Wear of Tailored Forming Steels

Timm Coors,\* Yusuf Faqiri, Felix Saure, Florian Pape, Thomas Hassel, and Gerhard Poll

This study investigates the wear behavior of additively welded cladding layers on less wear-resistant base materials using plasma-transferred arc welding and laser hot-wire cladding. The cladding layers are made from atomized AISI 52100, AISI 5140, and a stainless steel with (0.52 wt% C, 0.9 wt% Si, 14 wt% Cr, 0.4 wt% Mo, 1.8 wt% Ni, 1.2 wt% V, bal. Fe) on unalloyed steel AISI 1022M as the base material. The specimens' microstructure and surface hardness are comparable with conventional specimens of monolithic AISI 52100 and AISI 4140, which is used as a reference. Tribometer tests are carried out in ball-on-disk configuration to investigate the wear resistance of the specimen. The multimaterial specimens show comparable wear behavior to their monolithic counterparts, and a good performance of the stainless specimen in pure sliding is proven. These findings suggest that additive manufacturing processes can be used to clad less wear-resistant base materials and achieve high wear resistance, making it possible to exploit the advantages of surface coatings under severe wear conditions.

## 1. Introduction

In many areas of technology, active surfaces are in tribological contact with each other. For example, highly loaded contacts occur in sliding and rolling bearings, gearboxes, or machines and processes, which usually interact with an intermediate, i.e., lubricant, and an ambient medium.<sup>[1]</sup> These tribosystems are characterized primarily by the operational variables of sliding velocity and Hertzian surface pressure.<sup>[2]</sup> If the lubricant film thickness is not sufficiently large to completely separate the two contact partners or if no lubricant is present at all, solid body contacts occur. As a result of continuous sliding, rolling, impact,


or drilling movements, increased wear develops. Wear is defined as the progressive loss of material in a tribological system.<sup>[3]</sup> It is divided into four basic wear mechanisms: surface disruption, abrasive wear, tribochemical reaction, and adhesive wear.<sup>[4]</sup> In surface disruption, alternating loads on the tribosystem lead to crack initiation and subsequent crack growth until final separation of particles occurs. In abrasive wear, the main component is microchipped by the roughness peaks of the harder mating component or by wear particles during third-body contacts. During tribochemical reaction, a change in chemistry occurs in the boundary zone of both contact partners as a result of friction-induced thermochemical activation. Adhesive wear describes the local welding of surface elements of different contact partners,

combined with a subsequent separation of the surfaces, where particles are torn out of the softer material when the local strength is exceeded and the bonding force between the contact partners is not reached.

In addition to reducing frictional losses, minimizing wear is a frequent design goal in the development of efficient machines. For example, 59% of bearing failures occur as a result of lubrication failure or contamination of the lubricant.<sup>[5]</sup> The most common types of failure are due to abrasive wear (26%), surface fatigue (16%), and adhesive wear (7%). The resistance of a solid body to these surface-initiated wear mechanisms is called wear resistance.<sup>[6]</sup> Wear resistance can be determined for a tribological system on a material-specific basis by means of (mostly standardized) wear tests on tribometers, as overview, see, for example.<sup>[7,8]</sup> The most common application form of tribometers is setups with conformal contact geometry in pin-disk or ball-disk arrangement.<sup>[1]</sup> Contraformal contact geometries, such as two-disk or four-ball devices, are used less commonly and then primarily for lubricant characterization. An international round-robin test was carried out by Czichos, Becker, and Lexow<sup>[9]</sup> to determine repeatability and reproducibility in friction and wear tests. Ball-on-disk setup was used with aluminum oxide (Al<sub>2</sub>O<sub>3</sub>) and bearing steel AISI 52100 (material number: 1.3505) as tribomaterials. This allowed reference measurement data to be generated for the tribological material pairings investigated under defined test conditions. This in turn led to the creation of standardized ball-on-disk tests in ASTM G99<sup>[10]</sup> and DIN 50324 (withdrawn).<sup>[11]</sup> The reproducibility of friction data in ball-on-disk testing can be subject to relative standard deviations of  $\pm 20\%$  and more, see refs. [9,12,13]. Provided that the tests are performed under controlled conditions, a fluctuation in friction

T. Coors, F. Saure, F. Pape, G. Poll  
Institute of Machine Design and Tribology  
Leibniz University Hannover  
An der Universität 1, Garbsen 30823, Germany  
E-mail: coors@imkt.uni-hannover.de

Y. Faqiri, T. Hassel  
Institute of Materials Science  
Leibniz University Hannover  
An der Universität 2, Garbsen 30823, Germany

 The ORCID identification number(s) for the author(s) of this article can be found under <https://doi.org/10.1002/adem.202201740>.

© 2023 The Authors. Advanced Engineering Materials published by Wiley-VCH GmbH. This is an open access article under the terms of the Creative Commons Attribution-NonCommercial-NoDerivs License, which permits use and distribution in any medium, provided the original work is properly cited, the use is non-commercial and no modifications or adaptations are made.

DOI: 10.1002/adem.202201740

data is due to interfering asperity (micro-)contacts, typical for dry friction tests.<sup>[14,15]</sup> Further, humidity has a strong influence on the repeatability of friction and wear results both in steel–steel and ceramic–steel contacts.<sup>[16]</sup> It has therefore to be controlled.<sup>[17]</sup> In addition to the initial test conditions such as normal force, contact geometry, sliding distance, and speed, the properties of the active surface have a high influence in tribo testing.<sup>[18]</sup> This includes manufacturing-induced parameters such as surface roughness<sup>[19,20]</sup> as well as inherent material properties like hardness, microstructure, and composition.<sup>[21–24]</sup> Steel materials account for a large proportion of the tribomaterials currently in use.<sup>[25]</sup> For example, steel is frequently used in the automotive industry, in wind turbines, or in industrial applications in general.<sup>[26–30]</sup> Different steels in particular show different results in terms of coefficient of friction and wear resistance depending on the operating conditions.<sup>[31]</sup> For other tribotechnical materials such as hard metals or hard composites, nonferrous alloys or polymeric materials, please refer to further literature.<sup>[32–38]</sup> Protective coatings, for example, applied through vacuum deposition or thermal spraying, lead to a reduction of wear and friction.<sup>[39]</sup> Recently research focused on multilayer coating with individual layer thicknesses in the nanometer range, showing improvements for low-friction and high-wear resistance.<sup>[40]</sup> Under abrasive wear, however, there is a risk that these thin layers, with a total layer thickness of  $\approx 0.1\text{--}50\ \mu\text{m}$ , might quickly wear out.<sup>[41]</sup> This can be improved within certain limits by selective adjustment of the element composition.<sup>[42]</sup> By means of additive manufacturing (AM) processes for metals, it is possible to apply thicker layers with locally adapted material properties in terms of hardness and wear resistance.<sup>[43]</sup> In this case, it is possible either to manufacture the entire component additively (e.g., by means of a powder bed process) or to locally apply a more wear-resistant material.<sup>[44]</sup> Deposition welding processes, for example, are suitable for this purpose. With this, material areas with low strength requirements can be clad with another load-adapted material, enabling material- and cost-efficient components with high functional integration. Tribologically loaded surfaces are increased in their wear-resistance by the deposition of hard, abrasive-resistant, or fatigue-resistant materials on a simpler base material. Possible applications include improving the tribological properties of rolling bearings or cylinder raceways.<sup>[45,46]</sup> A further application of deposition welding is the repair and improvement of rails.<sup>[47,48]</sup> Material selection plays a major role in these applications in conjunction with AM processes. It is necessary to resolve a conflict between material requirements such as strength, hardness, and good processability, usually through welding. Materials currently used for wear-resistant AM parts are mostly metals.<sup>[49]</sup> Currently, Fe-, Ni- and Co-based alloy powders or wires are widely used for laser cladding, for example.<sup>[50]</sup> Ceramics and metal-matrix composites also offer great potential by laser cladding, but further research is needed regarding manufacturing technology and defect-free application.<sup>[51]</sup> AM process parameters are influencing the microstructure of the claddings, which in turn changes the wear and corrosion resistance of the tribological system. Navas et al.<sup>[52]</sup> investigated a laser-clad Tribaloy T-800 on specimens made of AISI 304. They carried out tribological testing on block-on-ring and ball-on-disk setups. It was observed that the laser-clad layers achieved high hardness and presented good wear behavior in dry conditions, with a dimensional wear coefficient ( $k$ ) between one and two orders of magnitude lower than that of the substrate.

To improve the wear resistance of 35CrMo steel, Han et al.<sup>[53]</sup> clad by means of laser cladding different amounts of Fe-Cr3C2 on the surface of the substrate. This led to a formation of a microstructure with carbide particles, which increased the hardness and wear resistance of the substrate. Ji et al. investigated the wear behavior of high-vanadium high-speed steels (HVHSS).<sup>[54]</sup> Therefore, he tested HVHSS with different amounts of carbon (1.58–2.92 wt%) against a counter-face of 40Cr rings using a block-on-ring setup. He showed that the hardness in HVHSS increases linearly with the carbon contents and the wear rate decreases with hardness, but not in a linear manner. Furthermore, he found out that the wear behavior of HVHSS is influenced on the carbide size, the distance between carbides, and the hardness of the matrix. Scandian et al. investigated the sliding wear behavior of white cast irons with various contents of chromium (16, 24, 28, and 32 wt%) and molybdenum (0, 3, 6, and 9 wt%). He carried out tests on a pin-on-disk tribometer in dry conditions and investigated the pin height loss of the different alloys. The results showed that the volume fraction, morphology, distribution, and volume fraction of carbides are related to the amount of molybdenum and chromium and have an influence on the wear resistance.<sup>[55]</sup> Stoot et al. examined the influence of oxides on the friction and wear of alloys. They found out that the development of smooth oxide particles on the load-bearing areas of alloys can lead to significant reductions in coefficients of friction and wear rates. These oxide particles can significantly improve sliding solid surface contacts.<sup>[56]</sup> A general procedure to positively influence the microstructure of AM components is subsequent thermomechanical processing by forming.<sup>[57]</sup> So-called tailored forming aims to produce load-adapted AM components where subsequent forming optimizes the microstructure and results in near-net-shape production. Different AM technologies like plasma-transferred arc welding (PTA) using metal powders or laser hot-wire cladding are utilized for manufacturing multi-material semi-finished workpieces.<sup>[57,58]</sup> These are formed for example by die forging or cross-wedge rolling. It is then possible to produce gears, shafts, or complex forgings such as wishbones.<sup>[59,60]</sup> Furthermore, lightweight potential can be exploited when friction welding or co-extrusion is used to produce the multimaterial semifinished product.<sup>[61]</sup> This makes it possible to join aluminum and steel and then form them together, thus achieving high functional integration.<sup>[62]</sup> However, no wear characteristics have yet been determined for parts manufactured for Tailored Formed parts. The aim of this work is therefore to characterize and quantify the wear behavior under solid-state sliding friction of deposition-welded tailored forming materials. Based on this, the suitability of tailored forming as a manufacturing strategy for highly loaded tribosystems can be estimated. The research hypothesis is that a sufficiently thick cladding layer with at least 1 mm thickness can protect a simpler base material from wear under harsh tribological conditions. Based on this, it can be further verified whether adapted materials can achieve a higher wear resistance than the previous standard for rolling bearing steel.

## 2. Experimental Section

To test this hypothesis, the following experimental methodology was developed: Using deposition welding (Section 2.1), various steel powders (Section 2.2) were clad to a steel substrate,

formed by die forging, heat treated, and postprocessed. Steels such as AISI 52100 rolling bearing steel, which are suitable for abrasive applications due to their high hardness but are actually considered to be nonweldable, were used as cladding materials. In addition, two commercially available powder and wire materials were used, which have good weldability but do not quite fulfill the hardness requirements for bearing applications. The geometry of the specimen corresponds to the housing washers for cylindrical roller thrust bearings of type 81212. The specimens were characterized in terms of their material composition (Section 2.2.1), microstructure (Section 2.2.2), and surface properties (Section 2.2.3). Ball-on-disk tests were then carried out using balls of alumina as counterbodies, see Section 2.3. To verify the approach, the additively manufactured samples were compared with commercial AISI 52100 rolling-bearing steel as a reference.

## 2.1. Manufacturing Process

Different welding strategies were used for specimen fabrication. The samples H100, H45, and H41 (see Section 2.2 for material designation) feature a spiral welding process, as shown in **Figure A1**. The welding began from the center of the disk, whereby the weld was applied on the workpiece in the shape of a helix. Therefore, the weld torch was moving in a circular motion from the inside to the outside of the disk, until the entire surface of the disk was clad. The welding process took 7 min and 40 s, whereby the disk heated up to 760 °C. **Figure A2** exemplary shows the welding strategy for sample H56. The welding process began from the center of the disk. The welding torch moved with a slow welding speed of 0.1 m min<sup>-1</sup> toward the edge of the disk. During the movement of the torch, the welding parameters were increased constantly to avoid a blockage of the torch. After the torch reached the edge of the disk, the main welding process started. Here, the torch oscillated stationary between two points and at the same time the turn and tilt table rotated around the *z*-axis. The oscillation increased the dynamics of the weld pool, whereby the degassing of the melt averted pores. After the turn and tilt table was rotated 360°, the torch moved back to the starting point and the welding process was completed. The welding process took 5 min and 26 s, whereby the disk heated up to 700 °C. After welding, rings were cut out of the disks by water jet cutting. The hybrid semifinished product was then hot-formed by die forging to convert the welded structure into a finer-grained forming structure. Subsequently, a material-specific heat treatment was carried out. This consisted of heating in an electric chamber furnace followed by quenching in oil at room temperature. The specimens were subsequently tempered. The final specimen geometry was machined. The final specimen had the dimensions of a housing washer from the cylindrical roller thrust bearing type 81212 (inner diameter: 62 mm, outer diameter: 95 mm). Details of the respective manufacturing process could be found in the corresponding publication.<sup>[63–66]</sup>

## 2.2. Materials and Sample Preparation

As described earlier, the tailored forming process chain was followed, featuring a steel-to-steel material transition in the direction of the force.<sup>[57]</sup> Based on previous work, plasma-transferred arc welding was used to clad higher-strength steel onto plates made

of the unalloyed steel AISI 1022M (1.0460). To test the rolling bearing performance of hybrid components, the commercial bearing steel AISI 52100 (1.3505)<sup>[64]</sup> as well as the heat-treatable steels AISI 5140 (1.7035)<sup>[63]</sup> and AISI HNV3 (1.4718) was chosen, whereby AISI HNV3 was applied to the identical substrate material by laser wire cladding.<sup>[65]</sup> The mentioned steels are characterized by a high hardness and wear resistance. However, they are not corrosion resistant due to their low chromium content and therefore cannot be used in environments where increased humidity is present. Hence, a new powder alloy had been developed by mixing Höganäs Rockit 401<sup>[67]</sup> and 706<sup>[68]</sup> in a ratio of 5:1 to obtain a corrosion-resistance and wear-resistance alloy.<sup>[66]</sup> For comparison, commercially available bearing washers made of the classic rolling bearing steel AISI 52100 without material transition (monolithic) were procured. In addition, bearing washers made of monolithic AISI 4140 (1.7225) were manufactured and investigated. For consistent material designation in this article, the carbon content was used with the prefix *M* for monolithic and *H* for hybrid (i.e., clad) samples on AISI 1022M substrate, see **Table 1**.

### 2.2.1. Chemical Composition

In **Table 1**, the chemical compositions of all materials are given. The data were obtained using a SPECTROMAXx (SPECTRO Analytical Instruments GmbH, Kleve, Germany) spark spectrometer. For statistical validation, 18 measurements were taken per sample on the entire circumference of the bearing washer after testing. M100 as standard-bearing steel was mainly alloyed with Cr and microalloyed with Si and Mn. Mo and Ni contents were at low levels. The elemental composition was very homogeneously distributed over the sample and shows only a very small scatter. Analogously, M42 with its specific elemental composition exhibited similar alloying properties, with Mo occurring as an additional alloy. The substrate M22 is lightly alloyed with C and Si and had a slightly increased Mn content. Although H100 was welded, this series of samples showed a very similar material composition compared to M100. Only a slightly increased variance was noticeable. With regard to the material composition, it could be assumed that the materials were almost identical. The measured chemical composition of the samples M100 and H100 also lied within the standard DIN EN ISO 683-17<sup>[69]</sup> for AISI 52100. However, V was also detected in the measurements, although it is not listed in the mentioned standard. In contrast, H41 showed a slightly reduced C concentration regarding the standard DIN EN ISO 683-2.<sup>[70]</sup> M42, in contrast, corresponded to the standard DIN EN ISO 683-2. The sample H45 had a slightly low content of 0.35 wt% C and 2.5 wt% Si. The standard DIN EN 10090 requires a minimum content of 0.4 wt% C and 2.7 wt% Si.<sup>[71]</sup> The sample H56 is the only alloy that has more than 13 wt% Cr and is, therefore, corrosion-resistant per definition.<sup>[72]</sup> This was also proven with corrosion tests, carried out in the study by Coors et al.<sup>[66]</sup> In summary, it can be said that the monolithic materials M100 and M42 corresponded to the standards in terms of chemical composition. In the case of the hybrid washers, only the H100 disk matched the standard, the disks of H45 and H41 had a lower C content. This may be due to a slight alloy burn-off or a higher degree of dilution due to the welding process, see.<sup>[63]</sup>

**Table 1.** Chemical composition as determined by optical emission spectrometry in wt%  $\pm 0.005$ ;  $N < 0.05$ ,  $P$  &  $S < 0.01$ . Name prefix: *M*: monolithic material specimen, *H*: hybrid sample with specified C content in the cladding on AISI 1022M substrate.

Sample	AISI	C	Si	Mn	Cr	Mo	Ni	V
M100	52100	0.95	0.29	0.34	1.57	0.03	0.12	0.01
M42	4140	0.41 $\pm$ 0.01	0.4	0.75	1	0.2	–	–
M22	1022M	0.22 $\pm$ 0.02	0.29	0.87	0.04	0.01	0.06	–
H100	52100	0.97 $\pm$ 0.04	0.31	0.41	1.61 $\pm$ 0.06	–	0.04	0.01
H56	–	0.52 $\pm$ 0.03	0.93 $\pm$ 0.06	0.27 $\pm$ 0.03	14.05 $\pm$ 1.18	0.39	1.79 $\pm$ 0.16	1.17 $\pm$ 0.11
H45	HNV3	0.30 $\pm$ 0.03	2.47 $\pm$ 0.1	0.36 $\pm$ 0.01	8.07 $\pm$ 0.22	0.02	0.11	0.04
H41	5140	0.35 $\pm$ 0.01	0.29	0.7	1.01 $\pm$ 0.01	0.04	0.12	–

### 2.2.2. Microstructure

Micrographs of the finished samples were taken for the qualitative characterization of the microstructure. The samples were ground with SiC paper and nylon cloth with diamond paste for polishing. For etching, a 2% HNO<sub>3</sub> solution was used to unveil the microstructure of the samples. Cross sections with a 1 $\times$  magnification are shown in **Figure A3**. They were sorted in descending order of C content. The cladding material was uniformly distributed and showed little dilution/mixing for H100, H56, and H41. For sample H45, the degree of mixing was higher because the local energy input, and thus the melt pool dynamics were lower in the case of laser beam welding. Also, a heat-affected zone was visible, which was very narrow for the PTA specimens H100, H56, and H41 after heat treatment (see in particular H100). From **Figure A3**, micrographs with 10 $\times$  and 100 $\times$  magnification are taken, see **Figure 1**. The large images in the background show the area of the material transition for the hybrid specimens. Depending on the manufacturing process, this area was about 1–3 mm below the specimen surface.<sup>[63–66]</sup> Due to the welding of the specimens, welding defects such as pores have occurred in some cases, see **Figure 1b,d** right. However, these flaws were located far enough away from the damage-relevant stresses in the near-surface area and could therefore be classified as noncritical for the present investigation. The near-surface area of interest was shown in each of the red boxes in the foreground of **Figure 1**. In delivery condition M100 (**Figure 1a**) showed a fine-grained martensitic structure with a certain share of retained austenite (see small darker areas) and tiny white primary spheroidized carbides.<sup>[73]</sup> In general, H100 looked quite similar, but the different areas were not equally distributed. Individual clusters of the previously described structures could be observed. During hardening, i.e., quenching and tempering, lath martensite was also formed close to the material transition to M22. Lath martensite occurred in lower C contents of about 0.4 – 0.6%.<sup>[74]</sup> The remaining substrate material is ferritic-pearlitic. The material transition was sharply defined and featured low mixing/dilution. This indicates that only negligible diffusion of C from the cladding layer into the substrate material occurs. H56 was characterized by a ferritic-martensitic structure with increased precipitation of Cr at the grain boundaries and a fine distribution of V and Cr carbides. A lath martensitic microstructure with retained austenite could be seen in H45.<sup>[75]</sup> A preferred orientation was not directly evident. The heat-affected zone was not as pronounced as with H100. The microstructure of M42 showed a

lath-tempered martensitic structure with uniformly distributed carbides at inter lath boundaries.<sup>[76]</sup> The microstructure of H41 was quite identical to M42, which was due to the similar chemical compositions. Just the amount of Mo was missing, whereby Mo led to increased carbide formation.<sup>[77]</sup>

### 2.2.3. Surface Hardness and Roughness

To create consistent conditions for the wear tests, all washers were finished on a modified laboratory grinder LABOPOL-5 (Struers A/S, Ballerup, Denmark). For this purpose, the specimens were loaded with 80 N and wet ground at 300 rpm in two steps. Between each step, a visual inspection was made to see if previous machining marks were no longer visible. The grinding parameters were: 1) diamond grinding wheel with grit 120 for 2 min and 2) diamond grinding wheel with grit 220 for 5 min.

For the finished parts, tactile roughness measurements were carried out with a Perthometer PCV system (Mahr GmbH, Göttingen, Germany). Four measurements in the circumferential direction and four measurements in the radial direction were taken for each washer with  $L_T = 5.6$  and  $L_C = 0.8 \times 5$ . The roughness values for each series of specimens are given in **Figure 2**. Across all steel disks, a roughness of  $\bar{R}_a = 0.08 \pm 0.02 \mu\text{m}$  was obtained with a unidirectional surface texture. This corresponds to the industrial standard of 81212 bearing washers. In addition, the hardness of the specimens was measured with 12 Rockwell measurements each according to DIN EN ISO 6508-1<sup>[78]</sup> on a ZHU 250 (ZwickRoell GmbH & Co. KG, Ulm, Germany) universal testing machine. The hardness values were converted following EN ISO 18265<sup>[79]</sup> and are also shown in **Figure 2**. This was taken just as indicative value, as hardness conversion was complex.<sup>[80]</sup> The industrial bearing washers (samples M100) featured a hardness of 62 HRC. For the welded specimen, H100 reached a higher hardness of 66 HRC due to the targeted heat treatment on a laboratory scale. Samples M42 and H56 featured a hardness of 58–60 HRC. In particular, H45 and H41 do not fulfill a usual minimum requirement of 58 HRC (> 650HV) for raceways of rolling bearings.<sup>[81–85]</sup> The substrate material showed a hardness of 165 HV1 before welding. After welding and combined heat treatment, a hardness of 250 HV1 was achieved in the base material.<sup>[64]</sup> In previous publications, it could be shown, that the hardness from cladding to substrate was homogeneous for each material investigated.<sup>[63–66]</sup> If the layer height of the coating layer was



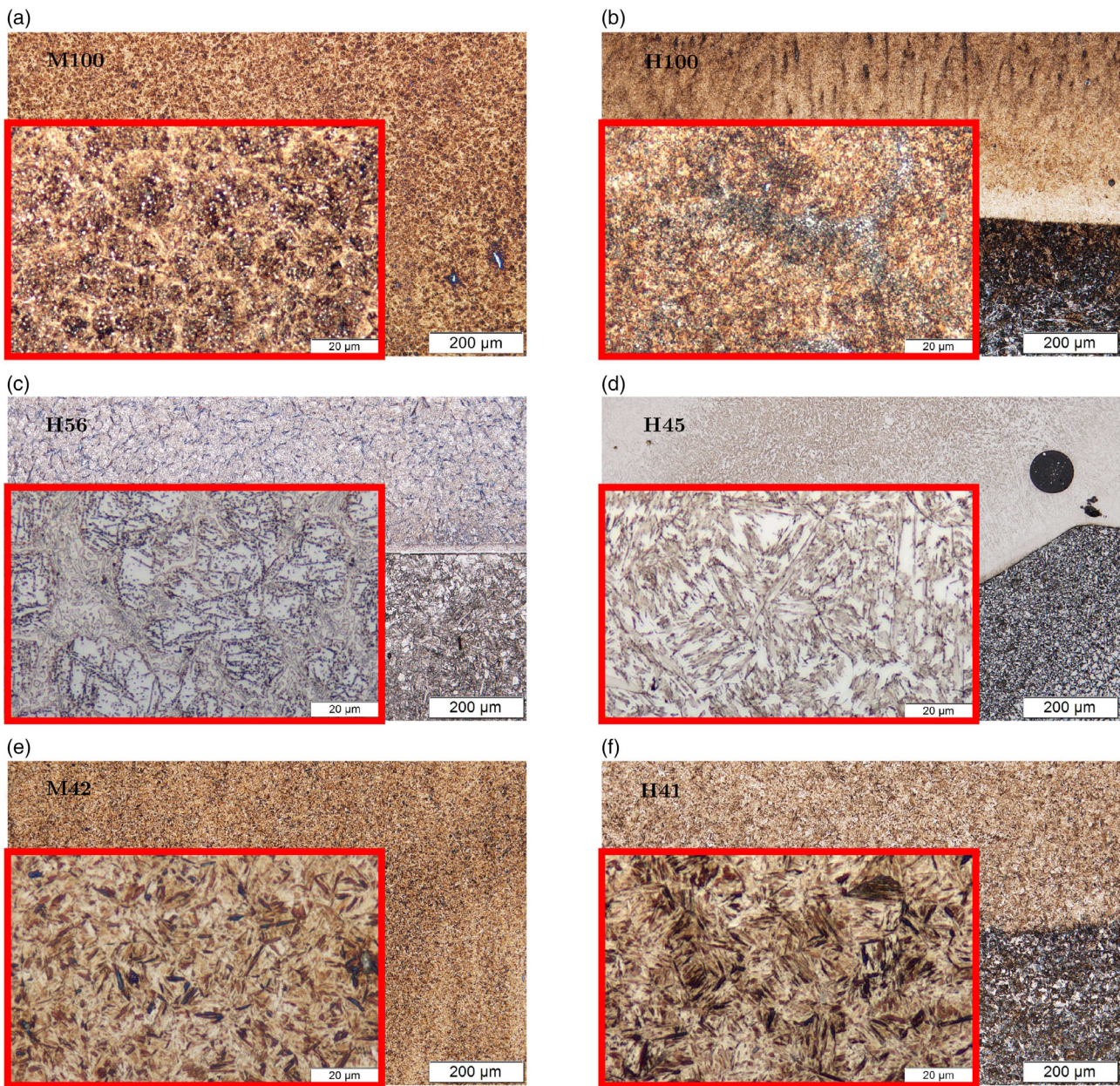


**Figure 1.** Micrographs after heat treatment and finishing with 10× magnification in the area of the material transition and 100× magnification of the cladding material in a near-surface area (red box): a) AISI 52100; b) welded AISI 52100; c) welded Rockit 401/706 mix 5:1; d) welded AISI HNV3; e) AISI 4140; and f) welded AISI 5140.

known or sufficiently large, the hardness at the surface corresponded in a first approximation to the hardness of the cladding or base material up to the material transition. It, therefore, is not assumed, that the material transition had an influence on wear and friction behavior. The  $\text{Al}_2\text{O}_3$  counterbodies featured a very high hardness of 1600 HV0.1.

### 2.3. Ball-on-Disk Testing

The wear of different material specimens under pure sliding were experimentally investigated on a ball-on-disk tribometer.

The dry friction tests were carried out in accordance with ASTM G99<sup>[10]</sup> and DIN 50 324 (withdrawn)<sup>[11]</sup> on a WAZAU TRM 5000 (Dr. Ing. Georg Wazau Mess- + Prüfsysteme GmbH, Berlin, Germany) tribometer. The tribometer was equipped with measurement systems for normal force, frictional torque, and speed. In addition, a wear measuring system measured the linear wear depth in the normal direction of the disk. The tests took place at laboratory air with a temperature of  $22 \pm 2^\circ\text{C}$  and approximately 50% humidity. The experimental setup is shown in **Figure 3**. Tailored forming disks with different material combinations were used as the specimens, see Section 2.2. The



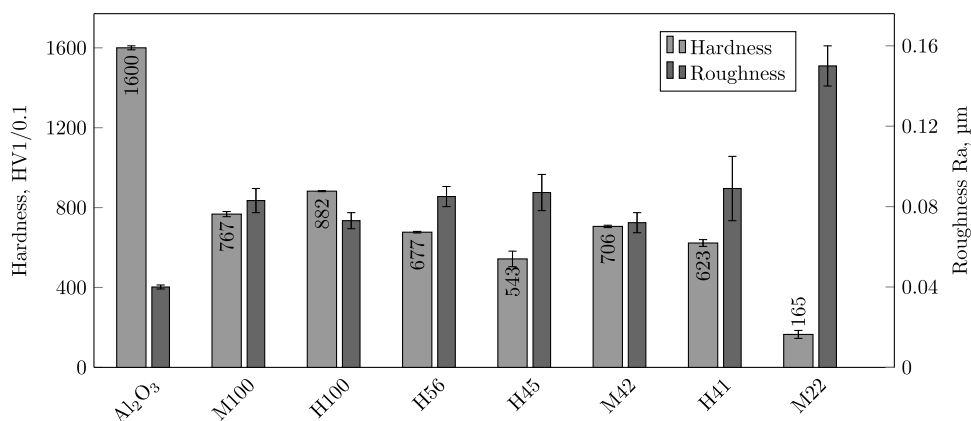


Figure 2. Hardness and roughness characteristics of the surface materials in tribocontact used.

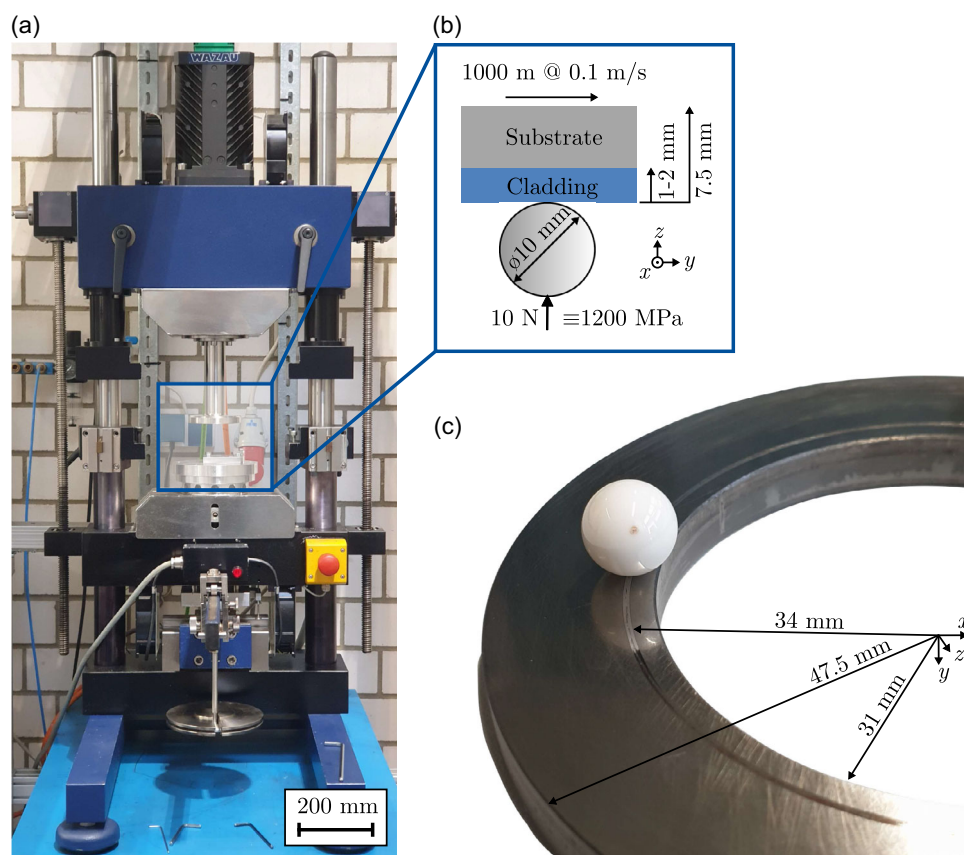


Figure 3. Experimental setup: a) ball-on-disk tribometer WAZAU TRM 5000 according to ASTM G99 and DIN 50324; b) sketch of the contact situation; c) ball-and-disk specimens with wear marks.

washers were mounted upside down in a three-jaw chuck on the spindle. It rotated at a constant speed of  $\bar{n} = 28.09 \pm 0.4$  rpm to achieve a sliding speed of  $v = 0.1 \text{ m s}^{-1}$  with a raceway radius of  $r = 34 \text{ mm}$ . To ensure that wear occurs on the steel disks, ceramic balls made of Al<sub>2</sub>O<sub>3</sub> with a diameter of  $d_b = 10 \text{ mm}$  in grade 25 according to DIN 5401<sup>[86]</sup> were used. These counter bodies were rigidly fixed in a stationary ball holder. The tests

were performed under a constant load of  $\overline{F}_N = 10.08 \pm 0.41 \text{ N}$  (see Figure A4) acting on the ball holder via a lever arm for a sliding distance of  $s = 1000 \text{ m}$ . The experimental deviation of about 4% during the test could be explained by small deviations in the axial runout of the disk with respect to the specimen holder and is considered here to be noncritical. In sphere-plane configuration, the Hertzian pressure was calculated to  $p_{\text{max}} = 1184 \text{ MPa}$ ,

considering the material properties of the contact partners ( $E_{\text{Al}_2\text{O}_3} = 380 \text{ GPa}$ ,  $E_{\text{steel}} = 210 \text{ GPa}$ ,  $\nu_{\text{Al}_2\text{O}_3} = 0.23$ ,  $\nu_{\text{steel}} = 0.3$ ). Three to five wear tests were carried out for each material.

### 3. Results

#### 3.1. Friction Behavior

Figure A4 shows the friction coefficients plotted over the wear distance for all tests of each material. The curves were obtained by smoothing the raw data of each individual test using a moving average filter with a fixed window length that is determined heuristically. For each material, the mean value was calculated from the smoothed data of all corresponding tests for this material. In addition, the error bars of these series and the overall mean value of all tests are plotted (black). It can be seen that the coefficient of friction (CoF) converges to a quasi-static value after a run-in period. For the steady phase in interval  $s_{\text{CoF}} = [200, 999] \text{ m}$ , the average CoF value has been calculated, see Table 2. The M100 and H100 series show

**Table 2.** Coefficient of friction (CoF) for the steady phase after run-in during ball-on-disk testing of different materials.

Sample	CoF	Sample	CoF	Sample	CoF
M100	$0.63 \pm 0.08$	H56	$0.59 \pm 0.15$	M42	$0.86 \pm 0.28$
H100	$0.63 \pm 0.03$	H45	$0.70 \pm 0.2$	H41	$0.92 \pm 0.46$
		Mean	$0.72 \pm 0.15$		

almost identical CoF. The material H56 shows a slightly lower CoF, than the above standard for rolling bearing steel, H45 is slightly above. All four materials mentioned are below the mean CoF value of all tests carried out (black line in Figure A4). Accordingly, the materials M42 and H41 show a higher CoF. The high CoF is due to the accumulation of debris particles between the M42/H41 disk and the  $\text{Al}_2\text{O}_3$  ball, which leads to three-body abrasive wear of the disk,<sup>[87,88]</sup> see Section 3.2.

#### 3.2. Ball Wear

After tribo-testing, the surface of the ceramic balls was examined optically on a VK-X210 laser scanning microscope (Keyence Corporation, Osaka, Japan). Depending on the tested material, little to no wear occurred on the balls. On all balls, more or less severe particle adhesions can be seen, some loose and some as agglomerates on the surface. In Figure 4, exemplary ball surfaces of H100, H56, and H41 contacts are shown. The sliding movement is from bottom to top. The most severe damage has occurred in contact with H41, see Figure 4c. The damage is about  $600 \times 800 \mu\text{m}$  in size and maximum  $13 \mu\text{m}$  deep. Based on the type and shape of damage, it can be supposed that the damage on the ball was caused by abrasive particles. Some of these particles are lying loose on the surface. Energy dispersive X-ray spectroscopic (EDX) measurements detected iron oxide compounds for these particles, see Appendix 4. At the run-out end of the contact, in contrast, elevations are measurable, which result from adhesive wear. For the ball of H41, the elevation height is about  $0.65 \mu\text{m}$ .

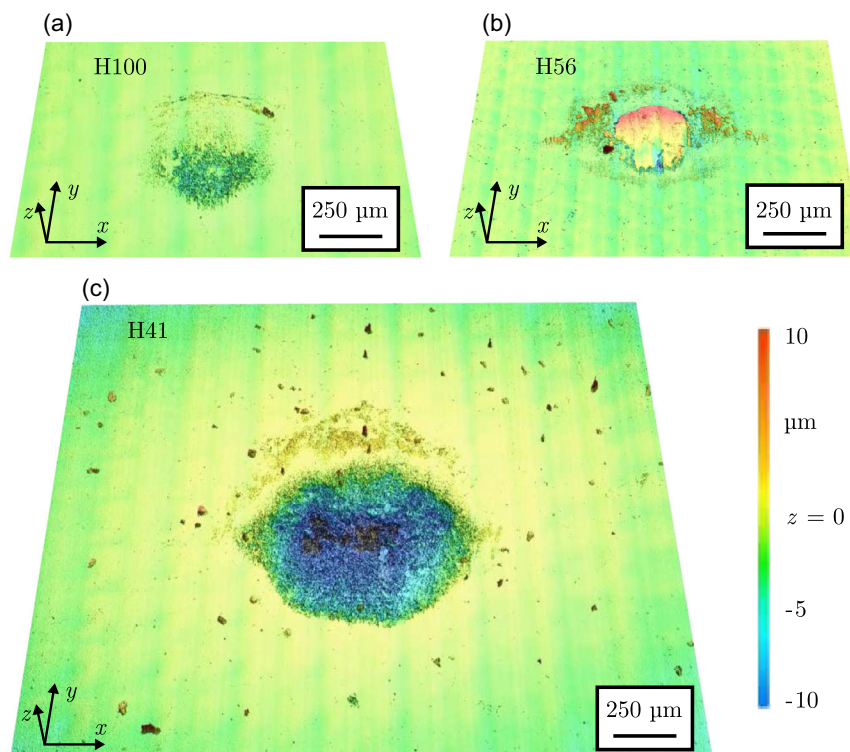


**Figure 4.** Wear marks acquired by means of laser scanning microscopy on  $\text{Al}_2\text{O}_3$  ball with three different counterparts: a) welded AISI 52100; welded Rockit 401/706 mix 5:1; and c) welded AISI 5140. The sliding movement is from bottom to top (positive  $y$ -direction).



The distance from the leading edge of the abrasive damage to the elevation is  $740\ \mu\text{m}$ . H100 shows a comparable, but much less severe damage. The abrasive damage area is  $380 \times 200\ \mu\text{m}$  in size and a depth of  $1.9\ \mu\text{m}$ . The build-up height of the adhesive damage is  $0.3\ \mu\text{m}$  here. The distance from the leading edge of the abrasive damage to the elevation is  $400\ \mu\text{m}$ . In contrast, only adhesive wear from the steel material to the ceramic ball has occurred with H56 in Figure 4b. A plateau of about  $230 \times 270\ \mu\text{m}$  has formed, rising steadily to about  $10\ \mu\text{m}$  in the direction of sliding. Adhesive particles are also present on both sides of the plateau and appear reddish under the reflected-light microscope.

### 3.3. Disk Wear Scars

When observing the ball surfaces, it was noticed that different wear phenomena can occur depending on the disk material. Micrographs of the disk's wear marks were taken after testing using laser scanning microscopy. The profile of the wear marks was measured for all disks. For this purpose, an approximately  $1 \times 3\ \text{mm}$  section was scanned at the positions  $0^\circ$ ,  $90^\circ$ ,  $180^\circ$ , and  $270^\circ$  for each disk. For each of these sections, a profile measurement was performed with 20 lines in an interval of  $50\ \mu\text{m}$  length. The profile average was then averaged over all the sections for each disk. The most severe wear marks for each material are shown in Figure 5 with

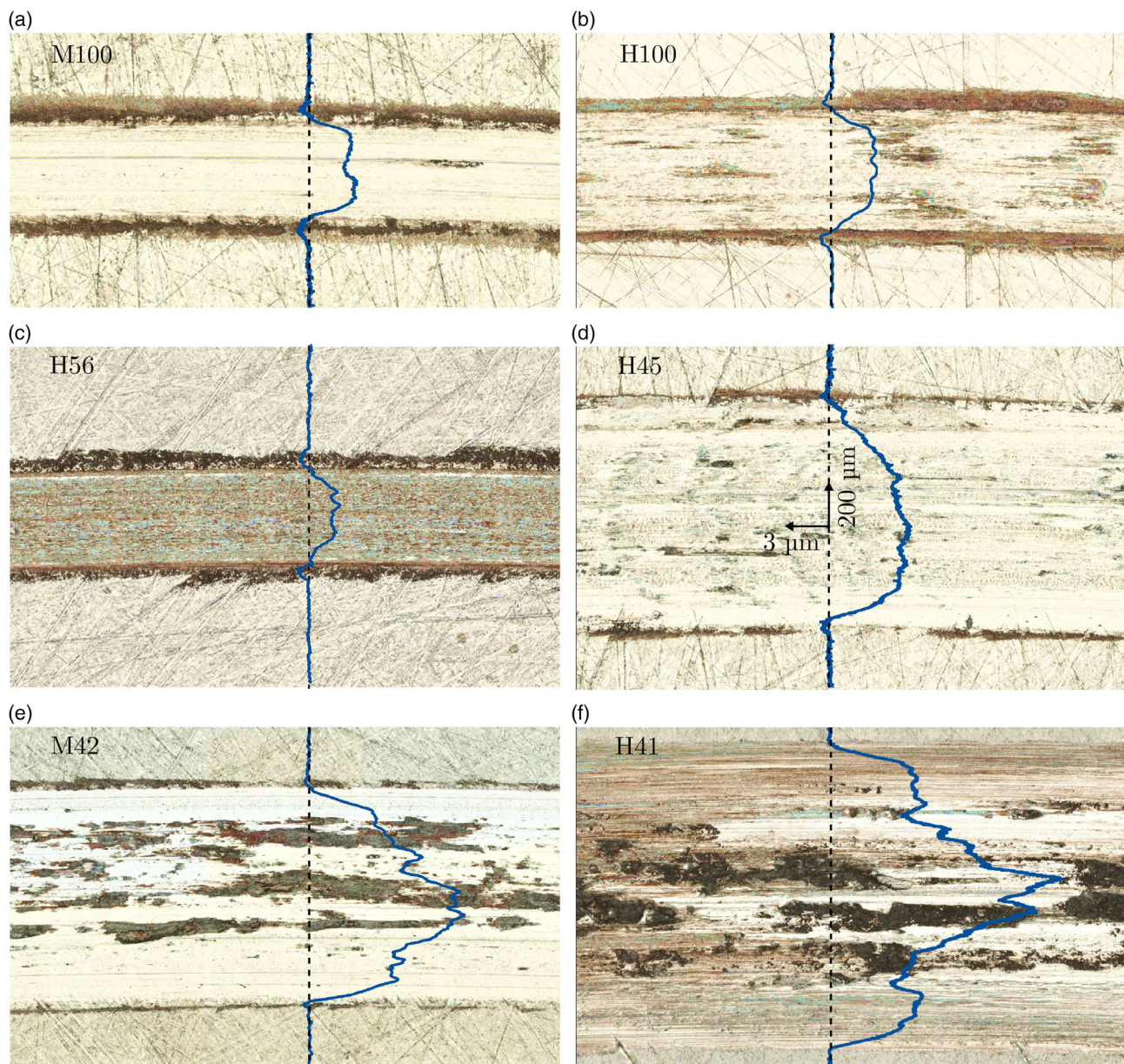


**Figure 5.** Micrograph and profile diagrams, both acquired by means of laser scanning microscopy, of averaged wear scars after experiment with  $\text{Al}_2\text{O}_3$  ball and following counterparts: a) AISI 52100; b) welded AISI 52100; c) welded Rockit 401/706 mix 5:1; d) welded AISI HNV3; e) AISI 4140; f) welded AISI 5140. Please note the different length scales for horizontal and vertical directions, depicted in (d).



their averaged profile. The abrasive contact between the steel disk and the ceramic ball leads to grooving of the disk. The wear profiles generally have an approximately semicircular shape, which differs in penetration depth and width of the wear track depending on the material. In addition, a material build up can be consistently detected at the edges of the track. Tribo-oxidation is partially detectable. Both AISI 52100 combinations M100 and H100 show a comparable wear mark. The wear tracks are about 200 μm wide and about 2 μm deep. The degree of smearing or tribo-oxidation is somewhat higher for H100. H56 has comparable geometric dimensions of the wear track (200 × 1.7 μm), but the visual appearance is different. H56 has a bluish and red-brown coloration, for which a tribochemical reaction could be responsible. The remaining samples all show more severe wear marks. In particular, H41 has the largest wear track in the entire test with 1000 μm width and 9 μm depth. In the profile plot in Figure 5f, it can be seen that the wear track has a very deep central region and is less deep at the edges. H45 and M42 show a smaller wear track in relation to H41. Compared to H45, the materials M42 and H41 show significantly more smearing. Energy dispersive X-ray spectroscopic line scans could prove increased O content with decreased Fe content in the outer areas and for the darker wear marks, see Figure A5.

### 3.4. Disk Wear Volume

With knowledge of the disks' wear track specifications, the disk wear volume can be determined according to ASTM G99.<sup>[10]</sup> For this purpose, the wear volume  $V_{W,disk}$  in [mm<sup>3</sup>] is calculated as the quotient of wear track radius  $r$  and track width  $b$  to sphere radius  $d_{ball}$  (all in [mm])

$$V_{W,disk} = \frac{\pi \cdot r_{\text{track}} \cdot b^3}{6 \cdot d_{\text{ball}}} \quad (1)$$

Note that this assumption is only valid if there is no 'significant' ball wear, as shown in Figure 4.<sup>[10]</sup> Figure 6 shows the wear volume in dependence of disk cladding material. Three tests of the five tests are shown in each case: the one with the highest

wear volume, the one whose wear amount corresponds most closely to the materials mean value, the one with the lowest wear, and the mean value including standard error. It can be seen that the results of Section 3.3 are confirmed. M100 and H100 show almost equal wear volumes. The stainless material H56 shows the lowest wear volume in the tests. Furthermore, the test results with this material are very consistent. The three remaining materials with a C content of more than 0.5% show larger wear volumes. Here, too, the stainless material H45 shows less scatter.

## 4. Discussion

The research hypothesis, stating that cladding layers can protect the base material from wear, could be confirmed. The cladding layers with a thickness of about 2 mm are in every case sufficient to withstand the loads in sliding contact. It is not assumed that a possible transition zone between the materials (i.e., heat-affected zone) has an influence on the friction and wear behavior. Thin wear protection coatings with thicknesses below 5 μm, produced, e.g., by vacuum-based coating processes or thin-film technologies, would not be sufficient for the experimental conditions presented here. The tests furthermore showed, that material hardness and wear strength correlate well in a first approximation. H41 and M41 are the softest materials and show the most pronounced (severe) wear behavior on average. In contrast, M100 and H100, as the hardest materials tested, show good wear behavior. However, this correlation does not truly hold for the steels with higher Cr content: H56 is not as hard as M100/H100 and still shows a very comparable or even lower wear volume, see Figure 6. Similarly, H45 is softer than M42/H41 but has a lower wear volume. To be able to describe and quantify this relationship without giving too much attention to the wear mechanism at hand, the Archard Model is used as a simple and frequently applied wear model in the following.<sup>[89]</sup> After transforming the traditional Archard equation, the dimensionless constant  $K$  can be determined as follows

$$K = \frac{V \times H}{F \times s} \quad (2)$$

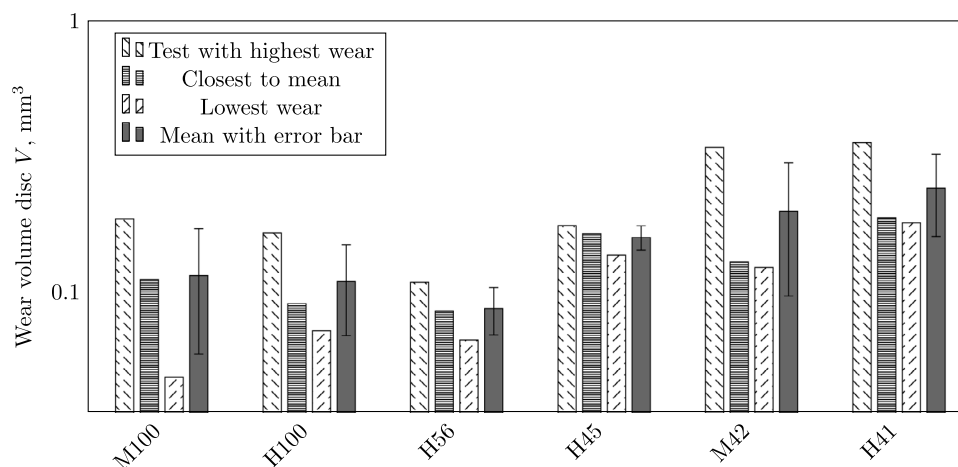
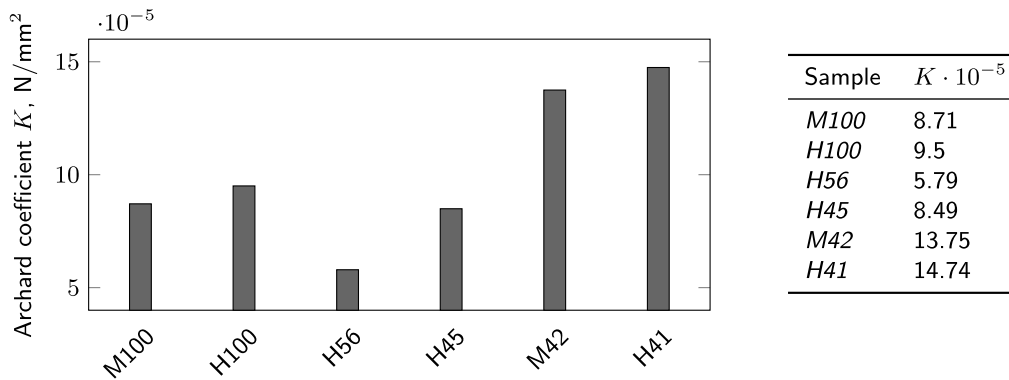


Figure 6. Wear volume of cladded steel disks.



**Figure 7.** Approximated Archard wear coefficient  $K$  for each material tested.

$K$  describes a material-dependent factor that is also referred to as the Archard wear coefficient. This factor is usually determined experimentally and is also dependent on test parameters such as surface roughness, hardness and hardening strategies, chemical bonding of the contact partners, and the like. Literature states a range of  $K = 10^{-8} \dots 10^{-3}$  for metals.<sup>[90]</sup> To determine  $K$ , the mean wear volume  $V = V_{w,disk}$  from wear testing of the various materials presented in Figure 6, is used.  $H$  gives the hardness of the softer contact partner, see Figure 2. The Vickers hardness number in ( $\text{kgf mm}^{-2}$ ) was converted to SI units ( $\text{N mm}^{-2}$ ) by multiplying the HV value by 9.807. The normal load  $F = F_N = 10 \text{ N}$  and the sliding distance  $s = 1000 \text{ m}$  are determined by the experimental conditions, see Section 2.3. In **Figure 7**, the Archard wear coefficient  $K$  is given for each cladding material tested.

It can be seen that H56 has the lowest Archard wear coefficient of  $K(H56) = 5.79 \times 10^{-5}$ . It is also lower than the next group of M100, H100, and H45, which have a wear coefficient of around  $K(100, H45) \approx 9 \times 10^{-5}$ . Steels M42 and H41 with a lower C content have a higher wear coefficient of  $K(M42, H41) \approx 14.25 \times 10^{-5}$ . The Cr-containing steels therefore cannot really be clustered with the other steels. Thus, the deviating Archard coefficient  $K$  in conjunction with the visual properties of the wear track indicates a different type of wear behavior. In contrast, this cannot be clearly delineated in the friction tests, as the data are subject to wide variation. It is possible that the Cr depositions together with the reduced C content generate fewer hard abrasive particles in the tribosystem with the  $\text{Al}_2\text{O}_3$  balls. As a result, there is less abrasive wear, which was also seen on the ball surface, cf. Figure 4. For H56, this may have additionally led to increased tribochemical oxidation, as indicated by the different coloration of the surface, cf. Figure 5. This may have been favored by the additional alloying elements Ni and V, resulting in the formation of a more favorable boundary layer. In conjunction with the carbide precipitates and the higher hardness of sample H56, better wear behavior was then observed. Hard Fe O composites damaged the other  $\text{Al}_2\text{O}_3$  balls and led to abrasive wear processes there. As described in Section 3.3, EDX suggests tribo-oxidation

and the formation of iron oxides for the low Cr materials in particular, see Section A4.

## 5. Conclusion and Outlook

This work focuses on wear investigations on a ball-on-disk tribometer for various cladding materials. The cladding was deposited additively by plasma-transferred arc welding of high strength, high carbon steel on mild steel. The specimens were subsequently hot formed for a more favorable microstructure, following the tailored forming approach. Summarizing the wear experiments, it can be said that the welded samples H100 (0.97 wt% carbon content) and H41 (0.35% C) are very comparable with their monolithic counterparts M100 (0.95% C) and M42 (0.41% C), respectively in terms of their specific wear behavior. This means that the welding process with subsequent forming has no significant influence on the wear behavior in pure sliding conditions. Ultimately, this finding offers the possibility to use better-performing materials for a specific use case like H56 (0.52% C, 14% Cr, 1.8% Ni, 1.2% V, bal. Fe), which can have additional advantages like corrosion resistance or good weldability. The reasons for the good performance of this material with comparatively lower wear are the high Cr content of the coating material and the better properties in the tribosystem with an  $\text{Al}_2\text{O}_3$  ball. By determining the Archard wear coefficient, which relates wear volume and material hardness to sliding distance at constant load, the good performance of H56 in pure sliding was confirmed.

In future investigations this material is to be used as raceways for a rolling bearing. Especially in roller thrust bearings or other applications with higher slide ratios, special materials like H56 can lead to improved performance. However, it is necessary to be able to select the right material for the specific application and to master the necessary manufacturing process to avoid defects in the workpiece.



## Appendix

### A.1 Welding Process

Figure A1 and A2.

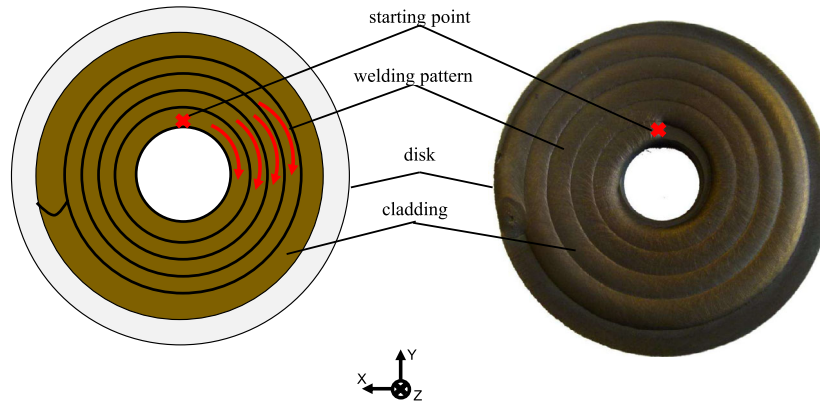


Figure A1. Spiral welding process.

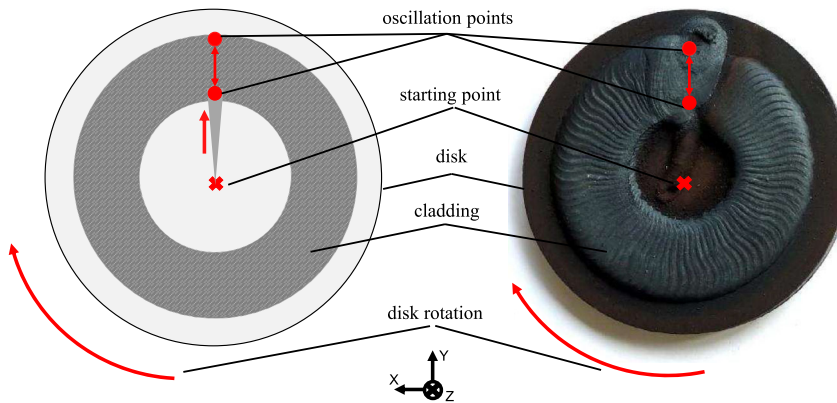


Figure A2. Welding process.

### A.2 Micrographs

Figure A3.

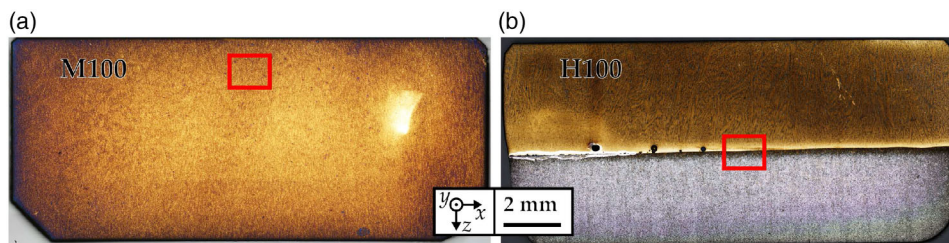


Figure A3. Cross sections: a) AISI 52 100; b) welded AISI 52 100; c) welded Rockit 401/706 mix 5:1; d) welded AISI HNV3; e) AISI 4140; and f) welded AISI 5140. The red box shows the magnified area shown in Figure 4.

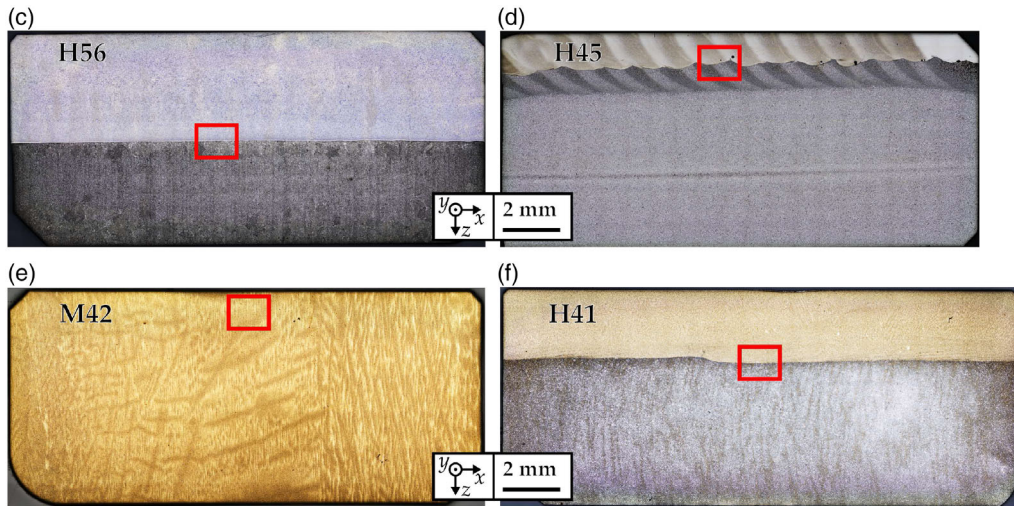


Figure A3. Continued.

### A.3 Friction

Figure A4.

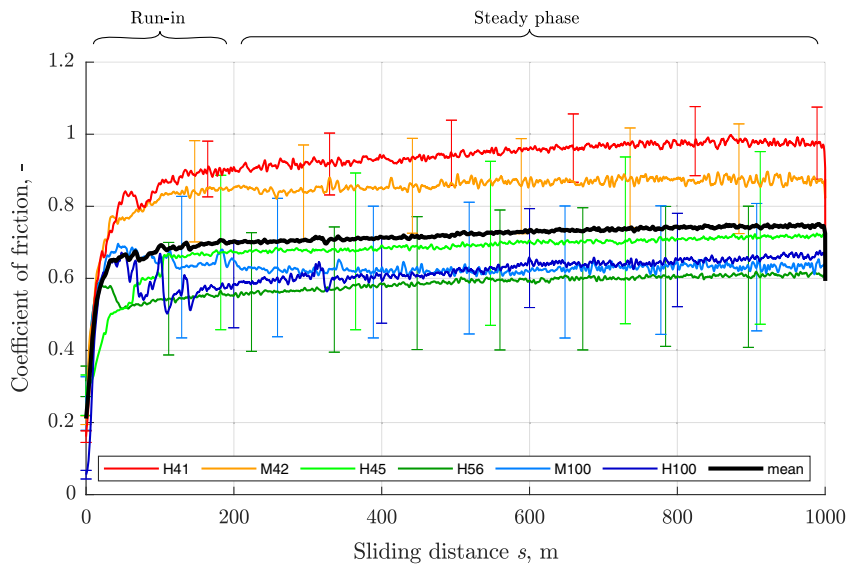


Figure A4. Coefficient of friction versus sliding distance as material-dependent mean with error bars of 3–5 tests per material and as overall mean across all measurements (black).



A.4 EDX

Figure A5.

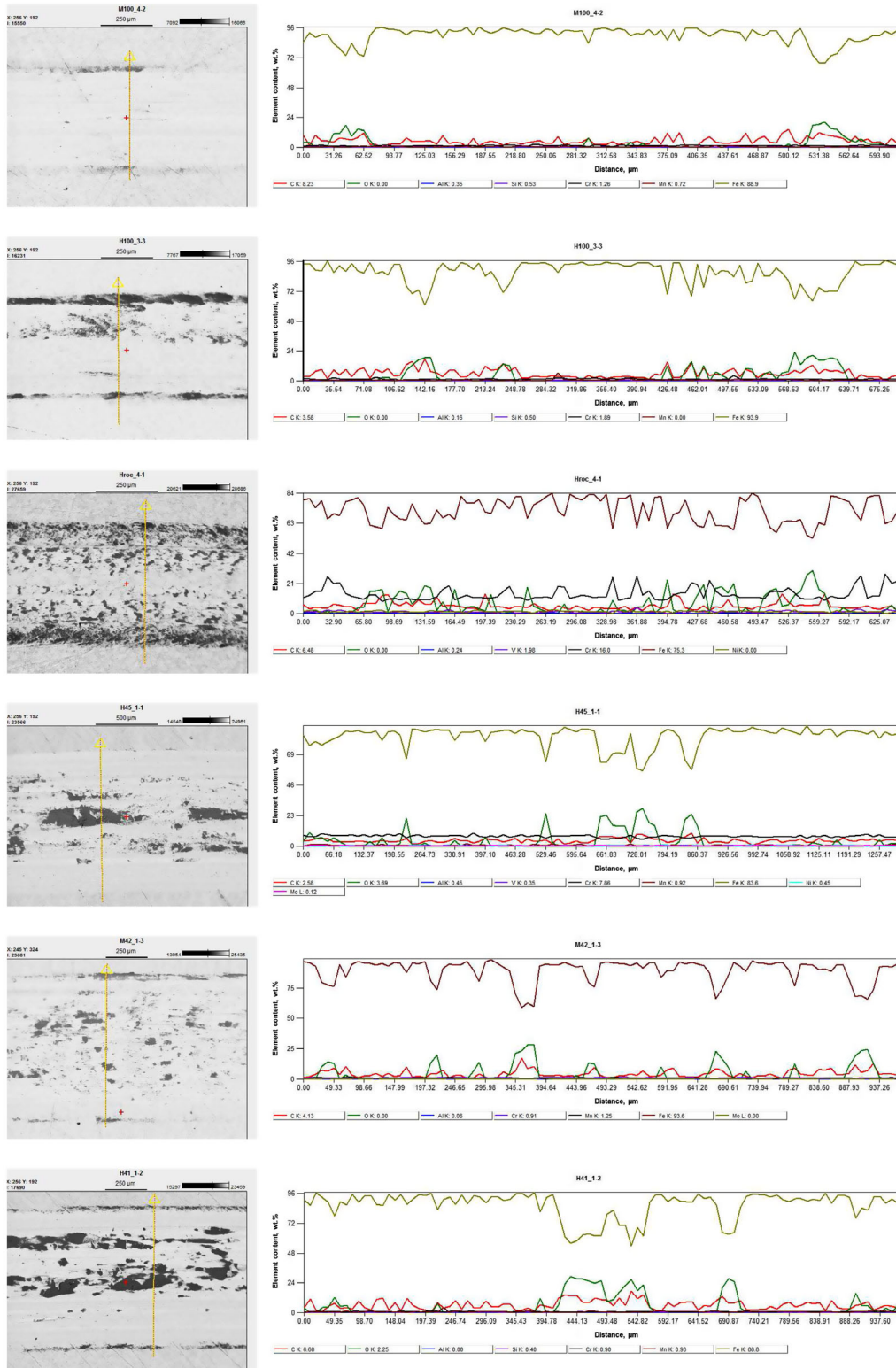


Figure A5. Energy dispersive X-ray spectroscopic line scans of wear tracks after testing.

## Acknowledgements

The results presented in this article were obtained within the Collaborative Research Centre 1153 “Process chain to produce hybrid high-performance components by tailored forming” in the subprojects A4, C3, and T1. The authors thank the German Research Foundation (DFG) for their financial support of this project under grant no. 252662854.

Open access funding enabled and organized by Projekt DEAL.

## Conflict of Interest

The authors declare no conflict of interest.

## Data Availability Statement

The data that support the findings of this study are available from the corresponding author upon reasonable request.

## Keywords

additive manufacturing, hybrid bearing, Rockit, stainless bearing, tailored forming, wear testing

Received: March 7, 2023  
Published online: May 1, 2023

- [1] *Tribology-Handbook* (Eds: H. Czichos, K.-H. Häbig), Springer Fachmedien Wiesbaden, Wiesbaden **2015**.
- [2] M. M. Khonsari, E. R. Booser, in *Applied Tribology: Bearing Design and Lubrication*, 3rd ed., John Wiley & Sons Inc., Hoboken, NJ **2017**.
- [3] ASM International, *Metals Handbook - Volume 18: Friction, Lubrication, and Wear Technology*, 10th ed., ASM International, Materials Park, OH **2017**.
- [4] V. L. Popov, in *Contact Mechanics and Friction*, Springer Berlin Heidelberg **2017**.
- [5] D. Rodriguez, K. E. Meyers, Bearing Damage Analysis: ISO 15243 Is Here to Help You, <https://evolution.skf.com/bearing-damage-analysis-iso-15243-is-here-to-help-you/> (accessed: January 2023).
- [6] *Friction and Wear of Materials* (Ed: E. Rabibinowicz), Wiley-Interscience, Hoboken, NJ **1995**.
- [7] *Mechanical Wear Fundamentals and Testing, Revised and Expanded*, (Ed: R. J. Bayer), 2nd ed., CRC Press, Boca Raton, FL **2004**.
- [8] K. G. Budinski, in *MNL 56 Guide to Friction, Wear and Erosion Testing*, ASTM International, West Conshohocken, PA **2007**.
- [9] H. Czichos, S. Becker, J. Lexow, *Wear* **1987**, 114, 109.
- [10] ASTM, ASTM G99 - Standard Test Method for Wear Testing with a Pin-on-Disk Apparatus, Technical Report, ASTM International, West Conshohocken, PA **2017**.
- [11] DIN - Deutsches Institut für Normung e.V., DIN 50324 - Tribology; Testing of Friction and Wear Model Test for Sliding Friction of Solids (Ball-on-Disc System) - Withdrawn, Technical Report, Beuth Verlag GmbH, Berlin **1992**.
- [12] E. Almond, M. Gee, *Wear* **1987**, 120, 101.
- [13] N. Wallbridge, D. Dowson, *Wear* **1987**, 119, 3.
- [14] H. Zhai, Z. Huang, *Wear* **2004**, 257, 414.
- [15] T. L. Schmitz, J. E. Action, J. C. Ziegert, W. G. Sawyer, *J. Tribol.* **2005**, 127, 673.
- [16] D. Klaffke, *Wear* **1995**, 189, 117.
- [17] D. Klaffke, *Tribotest* **1995**, 1, 311.
- [18] G. Straffelini, in *Friction and Wear*, Springer Tracts in Mechanical Engineering. Springer International Publishing, Cham **2015**.
- [19] M. Sedlaček, B. Podgornik, J. Vižintin, *Wear* **2009**, 266, 482.
- [20] G. Liang, S. Schmauder, M. Lyu, Y. Schneider, C. Zhang, Y. Han, *Mater.* **2018**, 11, 237.
- [21] O. Modi, D. Mondal, B. Prasad, M. Singh, H. Khaira, *Mater. Sci. Eng.: A* **2003**, 343, 235.
- [22] B. K. Satapathy, J. Bijwe, *Wear* **2004**, 256, 797.
- [23] C. Viáfara, A. Sinatora, *Wear* **2009**, 267, 425.
- [24] L. Tang, C. Gao, J. Huang, H. Zhang, W. Chang, *Tribol. Int.* **2013**, 66, 165.
- [25] K. G. Budinski, S. T. Budinski, *Tribomaterials: Properties and Selection of Materials for Friction, Wear, and Erosion Applications*, ASM International, Materials Park, OH **2021**.
- [26] Y. Enomoto, T. Yamamoto, *Tribol. Lett.* **1998**, 5, 13.
- [27] L. I. Farfan-Cabrera, *Tribol. Int.* **2019**, 138, 473.
- [28] A. Dhanola, H. Garg, *Eng. Fail. Anal.* **2020**, 118, 104885.
- [29] F. Findik, *Mater. Des.* **2014**, 57, 218.
- [30] L. Deters, M. Proksch, *Wear* **2005**, 258, 7.
- [31] Y. Sahin, *Mat. Des.* **2006**, 27, 455.
- [32] I. M. Hutchings, *Mater. Sci. Technol.* **1994**, 10, 513.
- [33] *Handbook of Nanomaterials and Nanocomposites for Energy and Environmental Applications*, (Eds: B. P. Aramide, A. P. I. Popoola, E. R. Sadiku, F. O. Aramide, T. Jamiru, S. L. Pityana, In O. V. Kharisova, L. M. Torres-Martínez, B. I. Kharisov). Springer International Publishing, Cham **2021**, pp. 731–755.
- [34] X. Li, M. Sosa, U. Olofsson, *Wear* **2015**, 340–341, 31.
- [35] K. Friedrich, Z. Zhang, A. K. Schlarb, *Compos. Sci. Technol.* **2005**, 65, 2329.
- [36] K. Friedrich, *Research* **2018**, 1, 3.
- [37] A. Kurdi, L. Chang, *Lubricants* **2018**, 7, 2.
- [38] H. H. Parikh, P. P. Gohil, *J. Reinf. Plast. Compos.* **2015**, 34, 1340.
- [39] C. Donnet, A. Erdemir, *Surf. Coat. Technol.* **2004**, 180–181, 76.
- [40] M. Khadem, O. V. Penkov, H.-K. Yang, D.-E. Kim, *Friction* **2017**, 5, 248.
- [41] K. Holmberg, H. Ronkainen, A. Matthews, *Ceram. Int.* **2000**, 26, 787.
- [42] P. Grützmacher, A. Tolosa, C. Gachot, G. Song, W. Bo, V. Presser, F. Mücklich, B. Anasori, A. Rosenkranz, *ACS Nano* **2021**, 15, 8216.
- [43] N. Haghdaei, M. Laleh, M. Moyle, S. Primig, *J. Mater. Sci.* **2021**, 56, 64.
- [44] D. Herzog, V. Seyda, E. Wycisk, C. Emmelmann, *Acta Mater.* **2016**, 117, 371.
- [45] D. Hertzner, in *Bearing Steels: Into the 21st Century* **1998**, 471–471–25, <https://doi.org/10.1520/STP12146S>.
- [46] A. Weisheit, A. Gasser, G. Backes, T. Jambor, N. Pirch, K. Wissenbach, in *Laser-Assisted Fabrication of Materials* (Eds: J. D. Majumdar, I. Manna) Springer Series in Materials Science, Vol 161, Springer, Berlin Heidelberg **2013**, pp. 221–240.
- [47] J.-w. Seo, J. Kim, S.-J. Kwon, H.-K. Jun, *Int. J. Precis. Eng. Manuf.* **2019**, 20, 1207.
- [48] S. Lewis, S. Fretwell-Smith, P. Goodwin, L. Smith, R. Lewis, M. Aslam, D. Fletcher, K. Murray, R. Lambert, *Wear* **2016**, 366–367, 268.
- [49] D. Bourell, J. P. Kruth, M. Leu, G. Levy, D. Rosen, A. M. Beese, A. Clare, *CIRP Annals*. **2017**, 66, 659.
- [50] E. Birger, G. Moskvitin, A. Polyakov, V. Arkhipov, *Weld. Int.* **2011**, 25, 234.
- [51] L. Zhu, P. Xue, Q. Lan, G. Meng, Y. Ren, Z. Yang, P. Xu, Z. Liu, *Optics & Laser Technol.* **2021**, 138, 106915.
- [52] C. Navas, M. Cadenas, J. Cuetos, J. de Damborenea, *Wear* **2006**, 260, 838.
- [53] B. Han, M. Li, Y. Wang, *J. Mater. Eng. Perform.* **2013**, 22, 3749.
- [54] Y. P. Ji, S. J. Wu, L. J. Xu, Y. Li, S. Z. Wei, *Wear* **2012**, 294–295, 239.
- [55] C. Scandian, C. Boher, J. de Mello, F. Rézai-Aria, *Wear* **2009**, 267, 401.



- [56] F. Stott, G. Wood, *Tribol. Int.* **1978**, *11*, 211.
- [57] B.-A. Behrens, L. Overmeyer, A. Barroi, C. Frischkorn, J. Hermsdorf, S. Kaierle, M. Stonis, A. Huskic, *Prod. Eng.* **2013**, *7*, 585.
- [58] T. Blohm, M. Mildebrath, M. Stonis, J. Langner, T. Hassel, B.-A. Behrens, *Prod. Eng.* **2017**, *11*, 255.
- [59] A. Chugreeva, M. Mildebrath, J. Diefenbach, A. Barroi, M. Lammers, J. Hermsdorf, T. Hassel, L. Overmeyer, B.-A. Behrens, *Metals* **2018**, *8*, 898.
- [60] T. Coors, F. Pape, J. Kruse, T. Blohm, R. Beermann, L. Quentin, S. Herbst, J. Langner, M. Stonis, M. Kästner, E. Reithmeier, F. Nürnberger, G. Poll, *Int. J. Adv. Manuf. Technol.* **2020**, *108*, 2409.
- [61] S. E. Thüerer, J. Uhe, O. Golovko, C. Bonk, A. Bougoucha, C. Klose, B.-A. Behrens, H. J. Maier, in *Proc. of the 20th Int. ESAFORM Conf. of Material Forming*, **2017** p. 140002.
- [62] B.-A. Behrens, H. J. Maier, G. Poll, P. Wriggers, F. Aldakheel, C. Klose, F. Nürnberger, F. Pape, C. Böhm, A. Chugreeva, T. Coors, D. Duran, S. E. Thüerer, S. Herbst, J.-I. Hwang, T. Matthias, N. Heimes, J. Uhe, *Prod. Eng.* **2020**, *14*, 569.
- [63] B.-A. Behrens, A. Chugreev, T. Matthias, G. Poll, F. Pape, T. Coors, T. Hassel, H. J. Maier, M. Mildebrath, *Metals* **2019**, *9*, 232.
- [64] T. Coors, M. Mildebrath, C. Büdenbender, F. Saure, M. Y. Faqiri, C. Kahra, V. Prasanthan, A. Chugreeva, T. Matthias, L. Budde, F. Pape, F. Nürnberger, T. Hassel, J. Hermsdorf, L. Overmeyer, B. Breidenstein, B. Denkena, B.-A. Behrens, H. J. Maier, G. Poll, *Metals* **2020**, *10*, 1363.
- [65] F. Pape, T. Coors, A. Barroi, J. Hermsdorf, M. Mildebrath, T. Hassel, S. Kaierle, T. Matthias, A. Chugreev, A. Chugreeva, B.-A. Behrens, L. Overmeyer, G. Poll, *Tribol. Online* **2018**, *13*, 320.
- [66] T. Coors, M. Y. Faqiri, F. Saure, C. Kahra, C. Büdenbender, J. Peddinghaus, V. Prasanthan, F. Pape, T. Hassel, S. Herbst, F. Nürnberger, H. Wester, J. Uhe, B. Breidenstein, B. Denkena, B.-A. Behrens, G. Poll, H. J. Maier, *Coatings* **2022**, *12*, 1699.
- [67] A. B. Höganäs, Rockit 401 - Sustainable Solution to Replace Hard Chrome Plating, **2021**, —[https://www.hoganas.com/globalassets/download-media/sharepoint/brochures-and-datasheets—all-documents/rockit\\_rockit-401-sustainable-solution-to-replace\\_2275hog.pdf](https://www.hoganas.com/globalassets/download-media/sharepoint/brochures-and-datasheets—all-documents/rockit_rockit-401-sustainable-solution-to-replace_2275hog.pdf) (accessed: July 2022).
- [68] A. B. Höganäs, Rockit 606/706 – Combat impact and abrasive wear, **2021**, [https://www.hoganas.com/globalassets/download-media/sharepoint/brochures-and-datasheets—all-documents/rockit\\_rockit-606-706\\_2653hog.pdf](https://www.hoganas.com/globalassets/download-media/sharepoint/brochures-and-datasheets—all-documents/rockit_rockit-606-706_2653hog.pdf) (accessed: July 2022).
- [69] DIN EN ISO 683-17:2015-02, Für eine Wärmebehandlung bestimmte Stähle, legierte Stähle und Automatenstähle.- Teil\_17: Wälzlagerstähle (ISO\_683-17:2014); Deutsche Fassung EN\_iso\_683-17:2014, Technical Report, Beuth Verlag GmbH, Berlin **2015**, <https://www.beuth.de/de/-/225838931>.
- [70] DIN EN ISO 683-2:2018-09, Für eine Wärmebehandlung bestimmte Stähle, legierte Stähle und Automatenstähle.- Teil\_2: Legierte Vergütungsstähle (ISO\_683-2:2016); Deutsche Fassung EN\_iso\_683-2:2018, Technical Report, Beuth Verlag GmbH, Berlin **2018**, <https://www.beuth.de/de/-/291176306>.
- [71] DIN EN 10090:1998-03, Ventilstähle und -legierungen für Verbrennungskraftmaschinen; Deutsche Fassung EN\_10090:1998, Technical Report, Beuth Verlag GmbH, Berlin **1998**, <https://www.beuth.de/de/-/3360341>.
- [72] DIN EN 10020:2000-07, Begriffsbestimmung für die Einteilung der Stähle; Deutsche Fassung EN\_10020:2000, Technical Report, Beuth Verlag GmbH, Berlin **2000**, <https://www.beuth.de/de/-/27404233>.
- [73] R. Kawulok, I. Schindler, J. Sojka, P. Kawulok, P. Opěla, L. Pindor, E. Grycz, S. Rusz, V. Ševčák, *Crystals* **2020**, *10*, 326.
- [74] H. Kitahara, R. Ueji, N. Tsuji, Y. Minamino, *Acta Mater.* **2006**, *54*, 1279.
- [75] L. Budde, K. Biester, P. Merkel, M. Lammers, M. Kriwall, J. Hermsdorf, M. Stonis, B.-A. Behrens, L. Overmeyer, *Prod. Eng.* **2022**, *16*, 661.
- [76] R. Kreethi, C. Sivateja, A. K. Mondal, K. Dutta, *J. Mat. Sci.* **2019**, *54*, 11703.
- [77] W. Weißbach, M. Dahms, C. Jaroschek, in *Werkstoffe und ihre Anwendungen*, Springer Fachmedien Wiesbaden, Wiesbaden **2018** p. 146.
- [78] DIN - Deutsches Institut für Normung e.V., Metallic Materials - Rockwell Hardness Test - Part 1: Test Method, Technical Report, Beuth Verlag GmbH, Berlin **2016**.
- [79] DIN - Deutsches Institut für Normung e.V., Metallic Materials - Conversion of Hardness Values, Technical Report, Beuth Verlag GmbH, Berlin **2014**.
- [80] E. Broitman, *Tribol. Lett.* **2017**, *65*, 23.
- [81] E. V. Zaretsky, *Mater. Sci. Technol.* **2012**, *28*, 58.
- [82] T. Harris, J. H. Rumbarger, C. P. Butterfield, Wind Turbine Design Guideline DG03: Yaw and Pitch Rolling Bearing Life, Technical Report NREL/TP-500-42362, National Renewable Energy Laboratory, Golden, CO, **2009**, p. 969722.
- [83] N. S. K. Inc., *Rolling Bearings*, **2021**, <https://www.nsk.com/common/data/ctrGpdf/bearings/e1102m.pdf> (accessed: July 2022).
- [84] A. G. Schaeffler, Rolling Bearings -Technical Principles and Product Data for the Design of Rolling Bearing Arrangements, **2021**, [https://www.schaeffler.com/remotemedien/media/\\_shared\\_media/08\\_media\\_library/01\\_publications/schaeffler\\_2/catalogue\\_1/downloads\\_6/hr1\\_de\\_en.pdf](https://www.schaeffler.com/remotemedien/media/_shared_media/08_media_library/01_publications/schaeffler_2/catalogue_1/downloads_6/hr1_de_en.pdf) (accessed: July 2022).
- [85] SKF Group, Rolling Bearings, **2021**, [https://www.skf.com/binaries/pub12/Images/0901d196802809de-Rolling-bearings—17000\\_1-EN\\_tcm\\_12-121486.pdf](https://www.skf.com/binaries/pub12/Images/0901d196802809de-Rolling-bearings—17000_1-EN_tcm_12-121486.pdf) (accessed: July 2022).
- [86] DIN - Deutsches Institut für Normung e.V., Din 5401 - rolling bearings - Balls for Rolling Bearings and General Industrial Use, Technical Report, Beuth Verlag GmbH, Berlin **2002**, <https://www.beuth.de/de/norm/din-5401/51818357>.
- [87] M.-X. Shen, J.-P. Zheng, X.-K. Meng, X. Li, X.-D. Peng, *Sci. A* **2015**, *16*, 151.
- [88] P. Hariharasakthisudhan, K. Sathickbasha, B. Surya Rajan, V. Jayanthram, *J. Tribol.* **2020**, *142*, 011702.
- [89] J. F. Archard, *J. Appl. Phys.* **1953**, *24*, 981.
- [90] P. Wriggers, in *Computational Contact Mechanics*, 2nd ed., Springer, Berlin **2006**.